

# Mechanically Robust and Ion-Conductive Polyampholyte Elastomers via Dimeric Ionic Bonding

Taebin Kim, Kyeong-Seok Oh, Sejung Oh, Jong Gun Jung, Gwanho Kim, Woojoong Kim, Yeonji Kim, Jiwon Kim, Hyunseo Kang, Sang-Young Lee,\* and Cheolmin Park\*

The development of ionic materials with high ionic conductivity and mechanical strength is challenging. This study presents a novel synthetic strategy for the development of a mechanically robust and ionically conductive polyampholyte elastomer based on ionic dimers (IDs) with strong ionic bonds between imidazolium and sulfonate. Polymerization of ID monomers with a network that forms a cross-linking moiety results in a novel polyampholyte ID elastomer (IDE). The addition of lithium (Li) salts in the IDE substantially enhances the ionic conductivity up to  $0.82 \text{ mS cm}^{-1}$  with a high  $\text{Li}^+$  transference number ( $t_{\text{Li}^+}$ ) of 0.79. The mechanical properties of the IDE with Li salts are remarkable, with a tensile strength of 27.4 MPa and a Young's modulus of 211 MPa, outperforming previous polyampholyte elastomers. A resistive-type iontronic sensor using the IDE exhibited excellent sensitivity (gauge factor = 2.92) and reliable cycle performance ( $\approx 400$  cycles) under repetitive stress. The IDE serves as a polymer electrolyte in a pouch-type full cell, showing stable capacity at a high current density of 1.0 C (corresponding to  $4.0 \text{ mA cm}^{-2}$ ) under ambient conditions ( $25^\circ\text{C}$ , 0.2 MPa). This synthetic strategy offers a new approach for designing ionic materials with high conductivity and mechanical strength.

## 1. Introduction

In recent decades, the importance of polymer-based ionic materials has greatly increased in the fields of soft robotics,<sup>[1,2]</sup> ionic skin,<sup>[3–5]</sup> wearable electronics,<sup>[6,7]</sup> and energy storage technologies.<sup>[8,9]</sup> Polymer-based ionic materials require a range of desirable properties, including transparency, ionic conductivity, mechanical strength, and electrochemical stability. These materials play a significant role in advanced applications, such as solid-state batteries,<sup>[10,11]</sup> supercapacitors,<sup>[12,13]</sup> wearable electronics,<sup>[14,15]</sup> and soft actuators.<sup>[16,17]</sup> In particular, ionic gels and elastomers, which are being developed for their long-term stability and high performance in various applications, have attracted significant attention because they aim to achieve high ionic conductivity and mechanical strength.<sup>[18,19]</sup>

However, current ionic elastomers face several major limitations in terms of enhancing both their ionic conductivities and

mechanical properties. For instance, increasing the ion concentration to improve the ionic conductivity leads to increased flexibility of the polymer chains, resulting in a decrease in mechanical strength. Conversely, introducing polar functional groups into polymer chains not only enhances mechanical strength but also strengthens the interactions between polymer chains, increasing rigidity, raising the glass transition temperature, and ultimately reducing ionic conductivity. These characteristics serve as major factors limiting the performance in real applications such as energy storage devices and iontronic products.<sup>[20]</sup> Therefore, an innovative approach is required to simultaneously enhance the ionic conductivity and mechanical strength.

Various strategies have been reported to overcome the trade-off between ionic conductivity and mechanical strength in ionic elastomers. Representative approaches include the precise control of phase separation between the ion transport domain and the mechanical properties domain,<sup>[21–23]</sup> the regulation of ionic conductivity through macromolecular structures,<sup>[24–26]</sup> the formation of crosslinked networks via interactions between 3D network polymers and ions,<sup>[27–29]</sup> and the development of polyampholytes, which utilize ionic bonding structures between polymer chains to enhance both mechanical strength and ionic conductivity.<sup>[30,31]</sup> Polyampholyte research stands out

T. Kim, J. G. Jung, G. Kim, W. Kim, Y. Kim, J. Kim, C. Park  
Department of Materials Science and Engineering  
Yonsei University  
Seoul 03722, Republic of Korea  
E-mail: [cmpark@yonsei.ac.kr](mailto:cmpark@yonsei.ac.kr)

K.-S. Oh, S. Oh, H. Kang, S.-Y. Lee  
Department of Chemical and Biomolecular Engineering  
Yonsei University  
50 Yonsei-ro, Seodaemun-gu, Seoul 03722, Republic of Korea  
E-mail: [syleek@yonsei.ac.kr](mailto:syleek@yonsei.ac.kr)

S.-Y. Lee  
Department of Battery Engineering  
Yonsei University  
Seoul 03722, Republic of Korea

C. Park  
Spin Convergence Research Center  
Korea Institute of Science and Technology (KIST)  
Seoul 02792, Republic of Korea

The ORCID identification number(s) for the author(s) of this article can be found under <https://doi.org/10.1002/adma.202508670>

© 2025 The Author(s). Advanced Materials published by Wiley-VCH GmbH. This is an open access article under the terms of the [Creative Commons Attribution-NonCommercial](#) License, which permits use, distribution and reproduction in any medium, provided the original work is properly cited and is not used for commercial purposes.

DOI: 10.1002/adma.202508670

compared with other material approaches because of the unique supramolecular structure formed through inter- and intra-chain ionic bond complexation.<sup>[30]</sup>

Polyampholyte elastomers are often developed by blending ionic polymers with opposite charges, inducing ionic bonding between the polymer chains and forming a double-stranded ionic polymer structure.<sup>[31]</sup> This approach maintains mechanical strength through electrostatic interactions between polymer chains, while simultaneously exhibiting ionic conductivity owing to the presence of ionic charges subject to ion dissociation and ion migration.<sup>[32]</sup> Reported polyampholytes with high ion conductivity were fabricated with additional ion doping, making them potentially suitable for various applications, including strain sensors,<sup>[33–36]</sup> gel electrolytes,<sup>[37]</sup> and supercapacitors.<sup>[38]</sup> Furthermore, their use as dielectric materials without additional ion doping has been previously reported.<sup>[39–50]</sup> However, according to previous research (summarized in Table S5, Supporting Information), most conductive polyampholytes exhibit high stretchability but low mechanical strength. After blending the ionic polymers, the counter-ions dissociated from each ionic polymer may remain because of the low removal efficiency arising from the slow diffusion of ions. Additionally, the low ionic bond energy in the polyampholyte is responsible for its low mechanical stability.

In this study, we present novel ionic dimers (IDs) with strong ionic bonds between the imidazolium and sulfonate groups. Subsequent copolymerization of the IDs with the crosslinking moiety led to the development of a novel polyampholyte ID elastomer (IDE) with high mechanical strength. A high ionic conductivity of  $\approx 0.82 \text{ mS cm}^{-1}$  and a high  $\text{Li}^+$  transference number ( $t_{\text{Li}^+}$ ) of 0.79 were achieved by adding Lithium bis(trifluoromethanesulfonyl)imide (LiTFSI) salts to the IDE, where  $\text{Li}^+$  transport is facilitated with the ionic bonds in the IDE. The IDE with LiTFSI possessed excellent mechanical properties, with a tensile strength of 27.4 MPa and a Young's modulus of 211 MPa. The mechanically robust and conductive IDE with LiTFSI served as a resistive-type iontronic sensor, effectively responding with high sensitivity (gauge factor = 2.92) and maintaining a stable resistance under deformation ( $\approx 400$  cycles). Additionally, the IDE serves as a polymer electrolyte in a pouch-type all-solid-state battery (ASSB), exhibiting stable capacity at a high current density of 1.0 C (corresponding to  $4.0 \text{ mA cm}^{-2}$ ) under ambient conditions (25 °C, 0.2 MPa).

## 2. Result and Discussion

### 2.1. Preparation of IDEs and Physical Properties of IDs

To synthesize an ionic bond-based dimer in the monomeric state, counter ions were removed through a precipitation reaction by mixing cationic and anionic monomers (Figure 1a). As shown in Figure S1 (Supporting Information), the precipitated KBr salt generated from the mixture of cationic monomer (1-[2-acryloyloxyethyl]-3-butyl imidazolium bromide, [AEBI]Br) and anionic monomer (3-sulfopropyl acrylate potassium salt, K[SPA]) was effectively removed ( $\approx 99\%$ ) because acetonitrile is a poor solvent in KBr salt, resulting in a high-purity product (yield = 98.38%). As shown in Figure S2 (Supporting Information), the chemical structure of ID was characterized using  $^1\text{H}$  nuclear

magnetic resonance ( $^1\text{H}$  NMR) and  $^{13}\text{C}$  nuclear magnetic resonance ( $^{13}\text{C}$  NMR). The synthesized ID was then used to prepare an IDE through a copolymerization reaction that involved mixing a photo initiator and a chemical crosslinking agent (Figure 1a). Polymerization from ID to IDE was confirmed by the disappearance of the peak associated with the acrylate group in  $^1\text{H}$  NMR (Figure S3, Supporting Information).<sup>[51]</sup>

To calculate the ionic dissociation constant ( $\xi$ ) of the synthesized ID, the absolute diffusion coefficients shown in Figure 1b were used as input for the Nernst-Einstein equation, as detailed in the Electrochemical Characterization section of the Experimental Methods. More specifically, the  $\xi$  value was determined by using both electrochemical impedance spectroscopy (EIS) and pulsed-field gradient nuclear magnetic resonance (PFG-NMR).<sup>[52]</sup> First,  $\xi$  is estimated by using the ionic conductivity ( $\lambda_{\text{EIS}}$ ) measured from EIS and the molar conductivity ( $\Lambda_{\text{NE}}$ ) obtained from PFG-NMR. EIS is a fast experimental method for measuring the ionic conductivity of a system, and the conductivity measured using this method only includes the conductivity contributed by “free ions.” Conversely, PFG-NMR measures the average self-diffusion coefficients ( $D_+$  and  $D_-$ ) of ions without distinguishing ion pairing or aggregation, which can be used to calculate  $\Lambda_{\text{NE}}$ . In this case,  $\lambda_{\text{EIS}}$  was measured to be  $0.0549 \text{ mS cm}^{-1}$ , and the molar concentration of ID per unit volume ( $C_{\text{IL}}$ ) was  $0.95 \times 10^{-3} \text{ mol cm}^{-3}$ . Using the Nernst-Einstein equation, the calculated  $\Lambda_{\text{NE}}$  was  $6.39 \times 10^{34} \text{ e}^2 \text{ s kg}^{-1} \text{ mol}^{-1}$ . As a result, the  $\xi$  value was calculated to be 0.0035 (Figure S4c and Table S1, Supporting Information), indicating that this very low  $\xi$  value corresponds to a high degree of ionic bonding at room temperature, supporting the conclusion that a low  $\xi$  value corresponds to strong ionic bonding between the ionic species.<sup>[52]</sup>

To analyze the degree of ID polymerization without the chemical crosslinking agent (poly(ethylene glycol) diacrylate (PEGDA) (Figure 1c)), the molecular weight and polymer dispersity index (PDI) were measured by gel permeation chromatography (GPC). The molecular weight of the ID samples polymerized without a chemical crosslinking agent ( $M_n$ : number-average molecular weight,  $M_w$ : weight-average molecular weight,  $M_z$ : maximum-average molecular weight) is  $\approx 2733$ , 5815, and  $12\,346 \text{ g mol}^{-1}$ , respectively, and the PDI was measured at 2.127.

As shown in Figure 1d and Figure S5 (Supporting Information), the glass transition temperatures ( $T_g$ ) of the gels polymerized with PEGDA using the cationic monomer ([AEBI]Br) and the anionic monomer (K[SPA]) were measured using differential scanning calorimetry (DSC) and were found to be 1 and  $-48$  °C, respectively. In contrast, the  $T_g$  of the IDE polymerized with PEGDA is 47 °C. The high  $T_g$  of the IDE, which differs from the expected intermediate value between the  $T_g$  of the [AEBI]Br gel and the K[SPA] gel<sup>[53]</sup> is attributed to the restricted movement of the polymer chains due to the strong ionic bonding within the IDE.

### 2.2. Ionic Transport Properties of IDEs

As shown in Figure S6 (Supporting Information), IDE/LiTFSI was synthesized by introducing a LiTFSI salt into an ID solution containing PEGDA, a photo initiator, and a solvent, followed by analysis of its thermal and physical properties. The LiTFSI

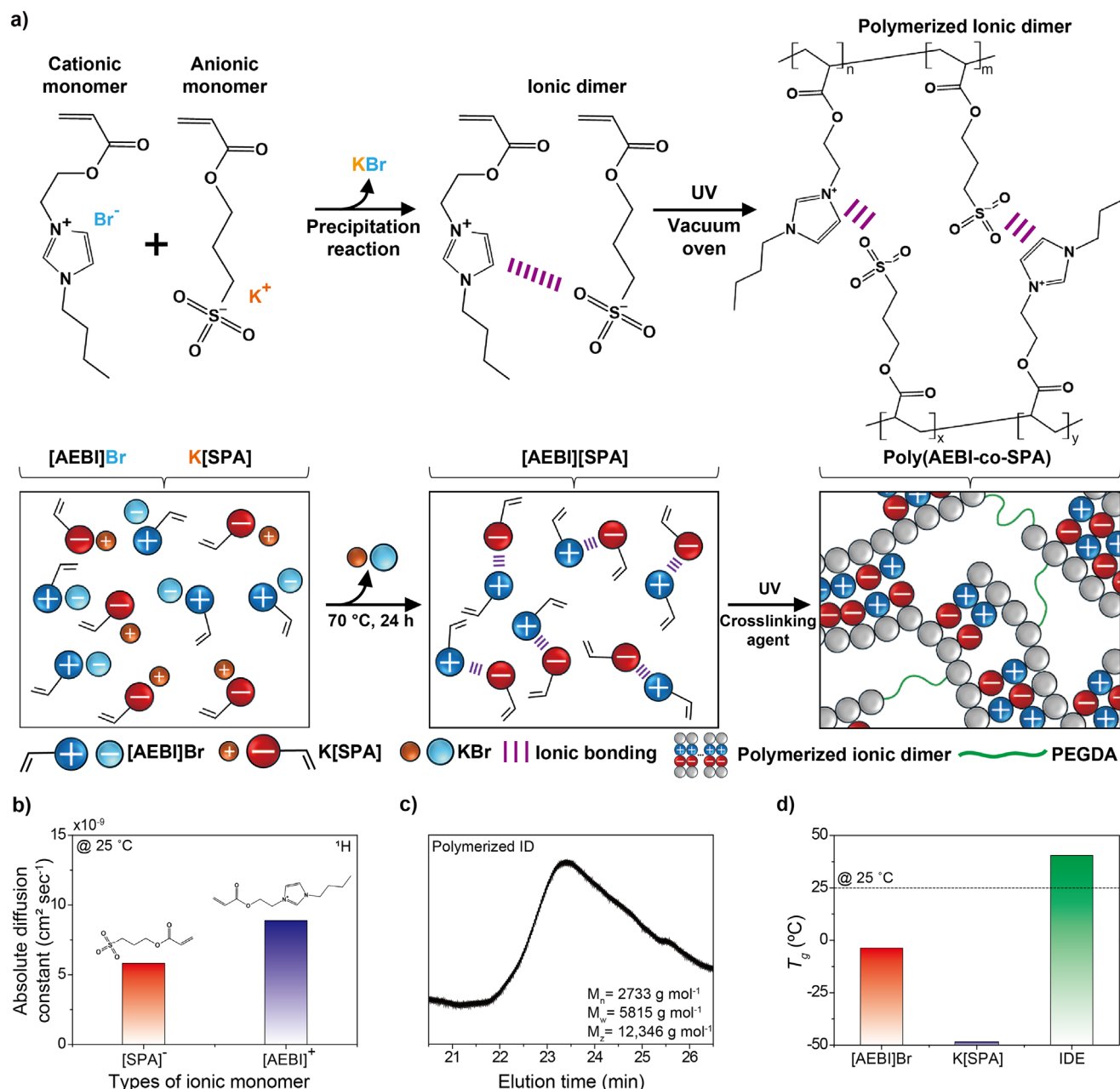


**Figure 1.** Preparation of IDEs and the physical properties of IDs. a) Schematic of the preparation process and structure of IDEs. The ionic monomers [AEBI]Br and K[SPA] are mixed and stirred at 70 °C for 24 h. The counter ion of Br<sup>-</sup> and K<sup>+</sup> is extracted by a precipitation reaction, and the obtained [AEBI][SPA] dimer is polymerized into IDEs through UV curing with a crosslinking agent. b) The <sup>1</sup>H self-diffusion coefficients of [SPA]<sup>-</sup> and [AEBI]<sup>+</sup> ionic monomers with PFG-NMR equipment at 25 °C. Inset: Chemical structure of [SPA]<sup>-</sup> and [AEBI]<sup>+</sup> ionic monomers. c) GPC elution curve of polymerized ID sample with deionized water as the solvent and poly(ethylene glycol)/poly(ethylene oxide) (PEG/PEO) as the standard. d) *T<sub>g</sub>* with DSC heating curve of [AEBI]Br, K[SPA], and IDE.

salt was incorporated based on the molar ratio of ID, where the molar ratio of LiTFSI (Y mol) to ID (X mol) was denoted as IDE/LiTFSI<sub>X/Y</sub> (mol/mol) (Table 1).

As shown in Figure S7 (Supporting Information), the IDE sample exhibited ≈68% transparency, which is attributed to the ionic bonding within its amorphous structure. Additionally, the IDE/LiTFSI<sub>1/2</sub> sample showed an increased transparency of ≈80% (both IDE and IDE/LiTFSI<sub>1/2</sub> samples have a thickness

of 500 μm). The thermal stability of IDE and IDE/LiTFSI<sub>1/2</sub> in ethanol was evaluated using thermogravimetric analysis (TGA) under a nitrogen atmosphere over a temperature range of 30–400 °C. Results indicated that IDE and IDE/LiTFSI<sub>1/2</sub> exhibited high thermal stability, with decomposition temperatures of ≈275 and 310 °C, respectively, and retained ≈5% residual solvent content up to 150 °C (Figure S8, Supporting Information).

**Table 1.** Composition of the IDE and LiTFSI used in this study.

Sample Code [IDE/LiTFSI_X/Y]	Molar Ratio [X/Y = ID/LiTFSI]	LiTFSI content [wt. %]	Physical state
IDE/LiTFSI_8/1	8:1	8.625	Solid
IDE/LiTFSI_4/1	4:1	17.25	Solid
IDE/LiTFSI_1/1	1:1	69	Solid
IDE/LiTFSI_1/2	1:2	138	Solid

To further investigate the  $T_g$  values of IDE and IDE/LiTFSI\_X/Y, DSC was performed. As shown in Figure S9 (Supporting Information), IDE exhibits a  $T_g$  of 47 °C, which is attributed to the strong ionic bonding within the polymer matrix (Figure 1d). As the concentration of LiTFSI increased, the plasticizing effect of the salt increased the flexibility of the polymer chain, resulting in a progressive decrease in  $T_g$ . Specifically, the  $T_g$  of IDE/LiTFSI\_X/Y decreases to 23, 5, −7, and −19 °C, respectively, as the LiTFSI content increases, demonstrating a clear trend of reduced  $T_g$  with higher LiTFSI composition.

To investigate the physicochemical interactions between the internal components resulting from the incorporation of LiTFSI into the IDE, attenuated total reflection Fourier transform infrared (ATR FT-IR) spectroscopy was performed. As shown in Figure 2a, the imidazole stretching and sulfonate symmetric stretching peaks of IDE appear at 1564 and 1034  $\text{cm}^{-1}$ , respectively (Figure S10, Supporting Information).<sup>[54,55]</sup> With increasing LiTFSI concentration, these peaks shift toward higher wavenumbers (blue shift), indicating strong interactions between the imidazole...TFSI<sup>−</sup> and sulfonate...Li<sup>+</sup> pairs. The pronounced interactions between the ionic bond network of IDE and the incorporated LiTFSI can be attributed to: (i) the high ion dissociation efficiency of LiTFSI and (ii) the enhanced Li<sup>+</sup> transport facilitated by the interactions with TFSI<sup>−</sup>.

The ionic conductivity of IDE/LiTFSI\_X/Y was measured to be 0.059, 0.076, 0.820, and 0.480  $\text{mS cm}^{-1}$ , respectively, with increasing LiTFSI compositions (Figure 2b). A decrease in conductivity was observed for IDE/LiTFSI\_1/2. PFG-NMR measurements further elucidated the relationship between the LiTFSI content and self-diffusion coefficients of Li<sup>+</sup> (Figure 2c; Figure S11, Supporting Information). Self-diffusion coefficients are presented as mean  $\pm$  S.E.M. ( $n = 3$ ). Statistical significance was assessed using the Kruskal-Wallis H-test. Exact p-values are provided in Table S2 (Supporting Information). The self-diffusion coefficients for IDE/LiTFSI\_X/Y were recorded as 1.548, 3.540, 9.232, and 7.655  $\text{cm}^2 \text{s}^{-1}$ , respectively, showing a trend that matches the ionic conductivity data in Figure 2c. However, in IDE/LiTFSI\_1/2, excessive LiTFSI content relative to the polymer chains impedes ion transport, resulting in reduced Li<sup>+</sup> self-diffusion coefficients and lower ionic conductivity. These results highlight the importance of balancing the LiTFSI content and polymer structure to optimize performance.

This result highlights the role of IDE in stabilizing the dispersion state of IDE/LiTFSI\_1/1. X-ray diffraction (XRD) analysis (Figure 2d) further supported these findings, as no significant crystalline peaks were observed in the XRD pattern

of IDE/LiTFSI\_1/1, whereas two distinct peaks at 24.68° and 28.53° appeared in the XRD spectrum of IDE/LiTFSI\_1/2, corresponding to the crystalline LiTFSI domains. These results collectively demonstrate that the optimized IDE structure promotes the uniform dispersion and enhanced dissociation of LiTFSI in IDE/LiTFSI\_1/1, further strengthening its potential as an advanced polymer electrolyte. The electrochemical performance of IDE/LiTFSI as a polymer electrolyte for ASSB applications was systematically evaluated, focusing on the correlation between the ion-bonding-based polymer chain structure of the IDE and its ion transport properties.

Meanwhile, dimethylformamide (DMF) has been used as an alternative solvent for IDE/LiTFSI to mitigate the electrochemical instability induced by ethanol<sup>[56]</sup> and reduce its reactivity with the Li metal anode in ASSBs.<sup>[57,58]</sup> IDE/LiTFSI\_1/1 prepared using DMF exhibited an ionic conductivity comparable to that of ethanol-based IDE/LiTFSI\_1/1 (Figure S12, Supporting Information). No noticeable differences were observed in the glass transition temperature ( $T_g$ ) and residual solvent content (Figures S8, S9, S13, and S14, Supporting Information), indicating that the solvent type had minimal impact on the final ion transport framework after solvent removal. In contrast, varying the IDE:LiTFSI molar ratio induced systematic and correlated changes in ionic conductivity (from 0.059 to 0.820  $\text{mS cm}^{-1}$ ) (Figure 2b),  $T_g$  (Figures S9 and S14, Supporting Information), and mechanical modulus (to be further discussed in Figure 3), reflecting a composition-driven structural evolution. Although the magnitude of ion conductivity changes induced by solvent and composition tuning may appear similar, their mechanistic origins are fundamentally different. Solvent variation exerts a negligible effect after solvent removal, whereas compositional tuning alters the polymer network architecture and associated ion transport properties.

The single-ion (Li<sup>+</sup>) conduction behavior of IDE/LiTFSI\_1/1, which exhibited the highest ionic conductivity (0.820  $\text{mS cm}^{-1}$ ), was assessed by measuring  $t_{\text{Li}^+}$  at room temperature using potentiostatic polarization. IDE/LiTFSI\_1/1 exhibited a high  $t_{\text{Li}^+}$  value of 0.79 (Table S3, Supporting Information), demonstrating the predominant contribution of Li<sup>+</sup> to ionic conductivity. Notably, this  $t_{\text{Li}^+}$  value is significantly higher than those of previously reported elastomeric ionic conductors (Figure 2e), highlighting the viability of the ionic bonding structure of IDE and the immobilization of TFSI<sup>−</sup> ions via imidazole groups (Figure 2a).

Further analysis using a Walden plot (Figure 2f) was conducted to investigate the ion transport efficiency influenced by the ionic bonding structure of the IDE. Additionally, the relationship between molar conductivity ( $\Lambda$ ) and glass relaxation time ( $\tau_g$ ) was examined.<sup>[59]</sup> The Walden plot of IDE/LiTFSI\_1/1 lies above the ideal Walden behavior line, indicating that the ionic bonding structure within the polymer chains of the IDE enhances ion transport. Notably, the IDE/LiTFSI\_1/1 exhibited superionic conduction behavior, comparable to that of (AgI)<sub>0.5</sub>–(AgPO<sub>3</sub>)<sub>0.5</sub>, with  $\tau_g \approx 100$  times faster than that of conventional PEO-based electrolytes at 25 °C. The detailed procedure for extracting  $\tau_g$  values via the time-temperature superposition method is described in Figure S15 (Supporting Information). For comparison, previously reported data for PEO<sub>9</sub>LiTFSI, PEO<sub>12</sub>LiTFSI, and superionic ceramic (AgI)<sub>0.5</sub>–(AgPO<sub>3</sub>)<sub>0.5</sub> electrolyte were used.<sup>[60,61]</sup> This result suggests that the ion transport in IDE, facilitated by the



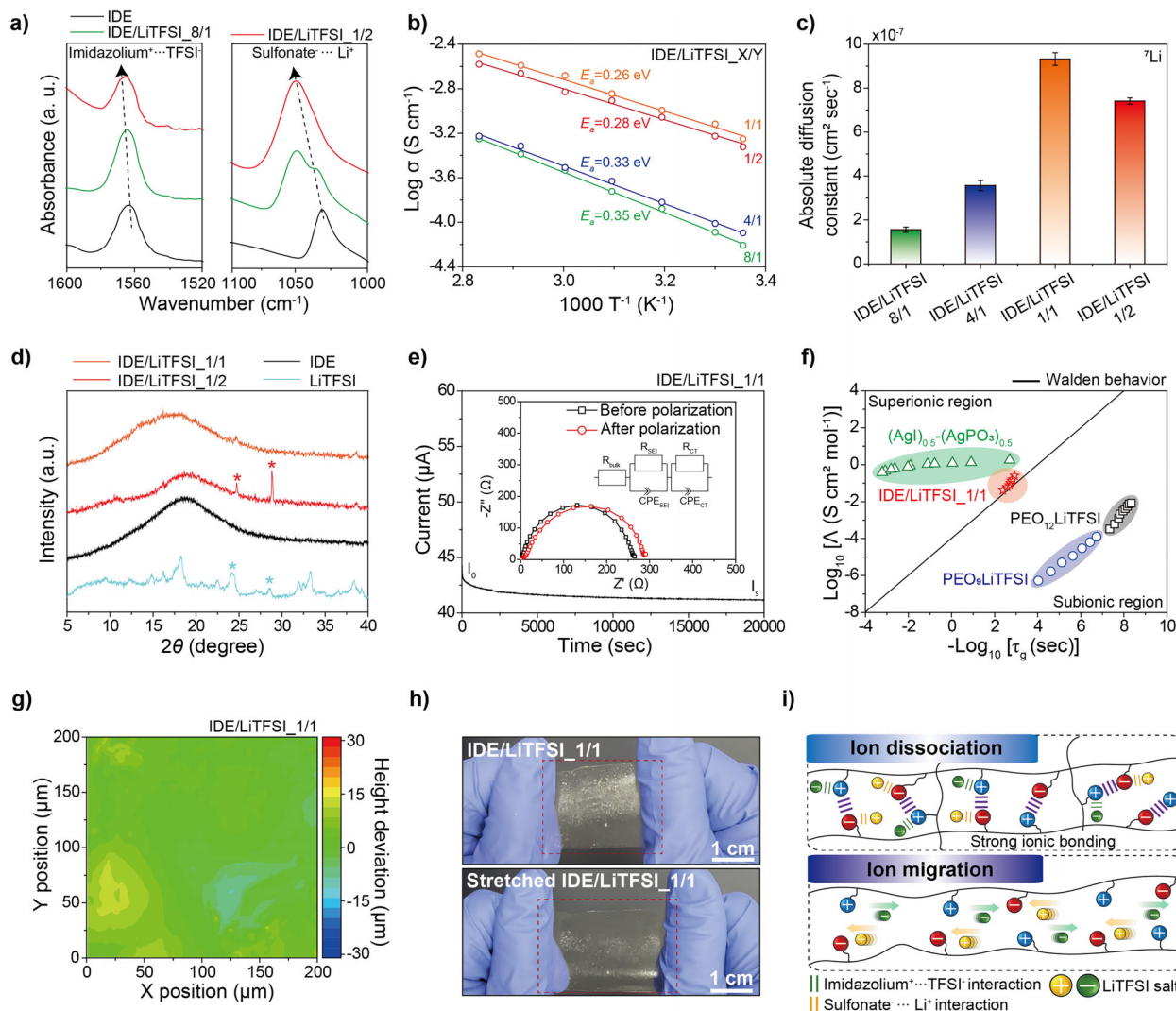


**Figure 2.** Properties of ionic behavior in IDEs. a) The FT-IR spectra of IDE and IDE/LiTFSI (Imidazole ring stretching peak: 1562 cm<sup>-1</sup>, SO<sub>3</sub><sup>-</sup> symmetric stretching peak: 1036 cm<sup>-1</sup>). b) Temperature dependence of ionic conductivity ( $\sigma$ ) and activation energy ( $E_a$ ) for IDE/LiTFSI\_X/Y. c) <sup>7</sup>Li<sup>+</sup> diffusion coefficient of IDE/LiTFSI\_X/Y through PFG-NMR. Data are presented as mean  $\pm$  S.E.M. ( $n = 3$ ). Statistical significance was assessed using the Kruskal-Wallis H-test. Exact p-values are provided in Table S2 (Supporting Information). d) XRD profiles of the IDE/LiTFSI\_1/1 (vs IDE/LiTFSI\_1/2). e) Time-dependent current profiles of IDE/LiTFSI\_1/1. Inset: EIS profiles for the Li||Li symmetric cell at 10 mV polarization of IDE/LiTFSI\_1/1. f) Walden plot showing  $\Lambda$  to  $\tau_g$  of IDE/LiTFSI\_1/1. The data of PEO<sub>9</sub>LiTFSI (from 25 to 65 °C), PEO<sub>12</sub>LiTFSI (from -35 to -5 °C) and (AgI)<sub>0.5</sub>-(AgPO<sub>3</sub>)<sub>0.5</sub> are taken from the literature.<sup>[60,61]</sup> and the solid line represents an ideal Walden line with a slope of 1. Copyright 2022. Reproduced with permission from the Royal Society of Chemistry.<sup>[60]</sup> Copyright 2022. Reproduced with permission from WILEY.<sup>[61]</sup> g) LSCM surface topography images of the IDE/LiTFSI\_1/1. h) The large-area and stretched photograph of IDE/LiTFSI\_1/1. i) Schematic illustration of ion dissociation and ion migration through the effect of ion bonding channels.

ionic bonding structure between the polymer chains, is fundamentally different from that of conventional polymer electrolytes, where ion transport is primarily governed by segmental polymer motion.

To investigate the effect of the IDE/LiTFSI precursor state on the dispersion uniformity of the IDE/LiTFSI\_1/1, laser scanning confocal microscopy (LSCM) analysis, which can map the surface roughness, was conducted. The deviation in the height of the IDE/LiTFSI\_1/1 over the wide range of the scanned area was negligible due to its well-dispersed precursor state (Figure 2g). As shown in Figure 2h, IDE/LiTFSI\_1/1 can be fabricated into large-area films (3  $\times$  5 cm<sup>2</sup>) while retaining its elastomeric prop-

erties, which allows for substantial stretchability. As illustrated in Figure 2i, the ionic bonding structure of the IDE enables high ion dissociation and efficient ion migration through interactions with LiTFSI, further validating its enhanced ion transport properties.

### 2.3. Mechanical Properties of IDEs

Figure 3 investigates the effect of the strong bonding strength of the ionic bonding structure in the IDE on its mechanical properties and evaluates the mechanical performance with

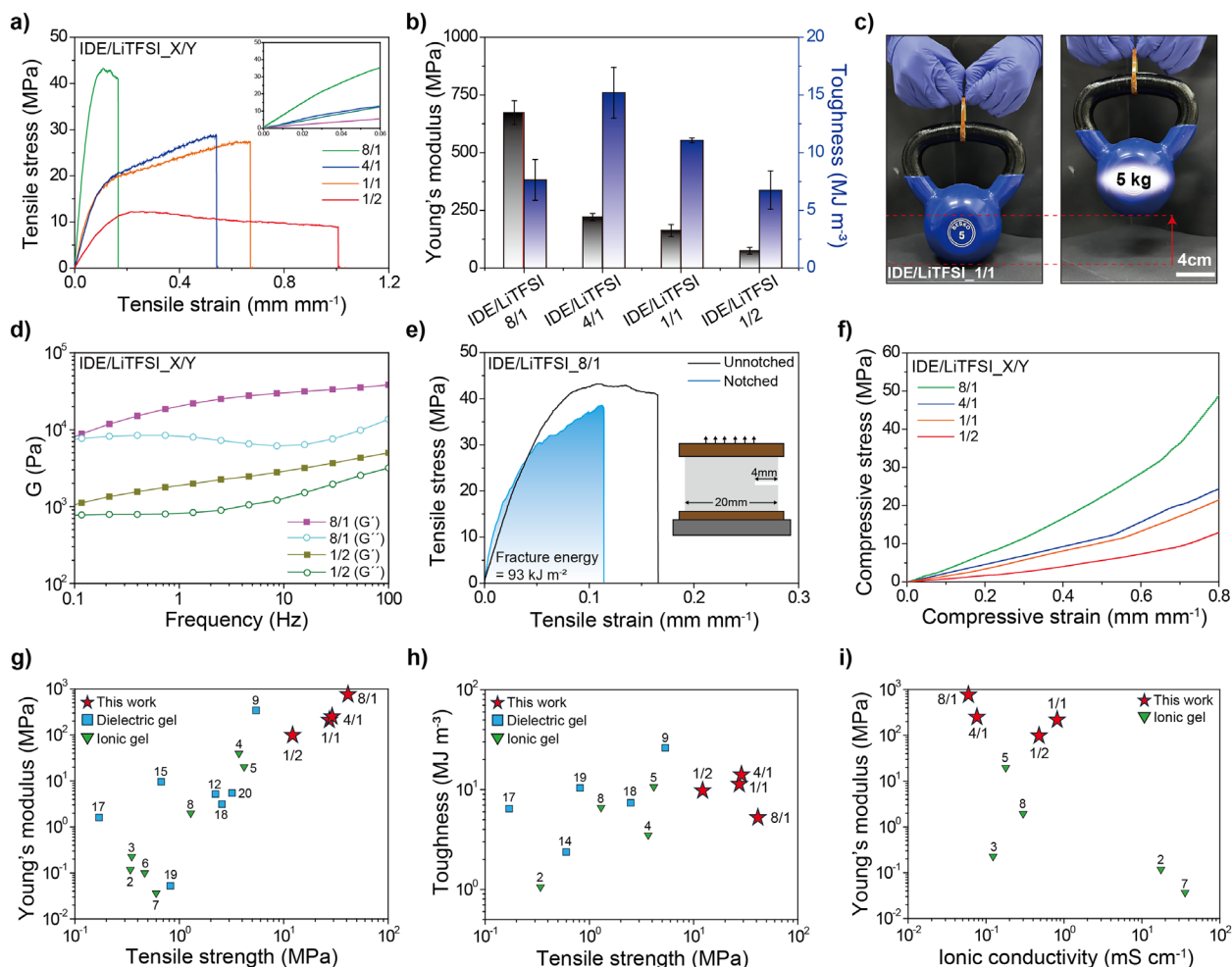


**Figure 3.** Mechanical properties of IDEs and comparison with other reported polyampholytes. a) Tensile stress-strain curves of IDE/LiTFSI\_X/Y. b) Comparison of the corresponding calculated Young's modulus and toughness of IDE/LiTFSI\_X/Y. Data are presented as mean  $\pm$  S.E.M. ( $n = 3$ ). Statistical significance was assessed using the Kruskal-Wallis H-test. Exact p-values are provided in Table S4 (Supporting Information). c) Photograph of the IDE/LiTFSI\_1/1 that can lift a 5 kg weight (IDE/LiTFSI\_1/1 size:  $4.0 \times 1.5 \times 0.2$  cm<sup>3</sup>). d)  $G'$  and  $G''$  of IDE/LiTFSI\_8/1 and IDE/LiTFSI\_1/2 in the frequency range of 0.1–100 Hz. e) Tensile stress-strain curves of notched samples of IDE/LiTFSI\_8/1 (linear notch, 20% of specimen width). f) Compression loading curves of IDE/LiTFSI\_X/Y (compression strain of 80%). Comparison of mechanical and ionic conductive properties of IDE/LiTFSI with reported polyampholyte, polyampholyte containing dielectric gel or ionic gel, including g) Young's modulus and tensile strength, h) toughness and tensile strength, and i) Young's modulus and ionic conductivity. The number assigned to each symbol corresponds to the serial number in Table S5 (Supporting Information).

varying LiTFSI salt content. As shown in Figure 3a, the tensile strength of IDE/LiTFSI\_8/1, 4/1, 1/1, and 1/2 decreased as the LiTFSI salt content increased, with values of 41.2, 28.7, 27.4, and 12.1 MPa, respectively. Furthermore, stretchability increased by 16%, 57%, 66%, and 100%, respectively. Increasing the LiTFSI salt content enhanced the flexibility of the polymer network, resulting in reduced mechanical properties. Despite the increase in LiTFSI salt content, the strong ionic bonding structure of the IDE retained its excellent mechanical properties. Additionally, the Young's modulus of IDE/LiTFSI\_8/1, 4/1, 1/1, and 1/2 was calculated to be 753, 243, 211, and 99 MPa, respectively, while the toughness was measured as 5, 14, 11, and 9 MJ m<sup>-3</sup>, respectively (Figure 3b). Mechanical properties (Young's modulus, toughness, tensile strength, and stretchability) are presented as mean  $\pm$  S.E.M. ( $n = 3$ ). Statistical signif-

icance was assessed using the Kruskal-Wallis H-test. Exact p-values are provided in Table S4 (Supporting Information). The IDE/LiTFSI materials exhibit a general plasticizing effect upon the incorporation of Li salt, indicating the potential for tunable mechanical properties. In particular, the IDE/LiTFSI\_8/1 sample showed a  $T_g$  of 23 °C in Figure S9 (Supporting Information), which is close to room temperature and leads to brittle behavior with low toughness. In contrast, the IDE/LiTFSI\_4/1 sample exhibited a significantly lower  $T_g$  of  $\approx 5$  °C, resulting in enhanced stretchability despite a moderate reduction in tensile strength, resulting in a marked increase in overall toughness. These findings indicate that the strong inter- and intra-chain ionic bonding network of IDE is retained upon LiTFSI addition, enabling controlled tuning of mechanical strength in IDE/LiTFSI systems.

Figure 3c demonstrates the excellent mechanical properties of IDE/LiTFSI\_1/1 using a 5 kg weight. Figure 3d and Figure S16 (Supporting Information) show the results of variable-frequency rheology tests measuring the mechanical properties of IDE/LiTFSI\_X/Y in the frequency range of 0.1–100 Hz. Within this frequency range, IDE/LiTFSI\_X/Y exhibited storage modulus ( $G'$ ) and loss moduli ( $G''$ ), demonstrating a stable ionic bonding structure even with the addition of LiTFSI. Strong ionic bonding between the polymer chains makes IDE highly resistant to crack propagation. This ionic bonding structure effectively relieves stress concentration at the crack tips. As shown in Figure 3e, notched IDE/LiTFSI\_8/1 demonstrated excellent resistance to crack propagation, withstanding up to 60% of maximum stretchability. Furthermore, the fracture energy ( $\Gamma$ ) of IDE/LiTFSI\_8/1 was  $93 \text{ kJ m}^{-2}$ , which is comparable to that of zinc alloys ( $<100 \text{ kJ m}^{-2}$ ), titanium alloys ( $<110 \text{ kJ m}^{-2}$ ), and other reported materials.<sup>[62,63]</sup> Figure S17 (Supporting Information) presents the notched IDE/LiTFSI\_8/1, further proving its low sensitivity to crack propagation. Figure 3f shows the compressive strength test results of IDE/LiTFSI\_X/Y. Compressive strength was measured up to a compressive strain of 80%, which showed a similar trend to the tensile test results. As the LiTFSI content increased, the compressive strength decreased.

Figures 2 and 3 demonstrate the correlation between the ionic behavior and mechanical properties of IDE/LiTFSI. The strong ionic bonding structure of the IDE enhances ion dissociation and ion mobility, while maintaining ionic interactions between polymer chains to improve mechanical properties. Compared to previous polyampholyte-based studies that aimed to achieve both ionic conductivity and mechanical performance using dielectric or ionic gels, this system exhibits clear advantages in terms of both mechanical strength and ionic conductivity (Figure 3g–i; Table S5, Supporting Information). More details are provided in Figure S18a–c (Supporting Information). In particular, the Young's modulus and ionic conductivity of the polyampholyte outperformed previously reported values, further confirming its excellent mechanical properties and ionic conductivity. Additionally, compared with previously reported ionic tough elastomers, IDE/LiTFSI demonstrated superior performance (Figure S18d–h, Supporting Information and Table S5, Supporting Information).

## 2.4. Adhesive Properties of IDE/LiTFSI

The ionic bonding structure of IDE/LiTFSI\_X/Y enables adhesion to various substrates by simply attaching the sample to the substrate to form a contact. Strong adhesion to various substrates is crucial for the stability, durability, and development of noninvasive devices in the iontronic field.<sup>[64]</sup> Additionally, it is a critical material property for ensuring electrode adhesion stability in energy storage devices, particularly in battery research, and for advancing flexible solid-state battery technologies.<sup>[65]</sup>

The IDE/LiTFSI\_8/1 sample demonstrated robust adhesion to glass, polyethylene terephthalate (PET), copper (Cu), and aluminum (Al) substrates without any surface pretreatment or modification (Figure 4a), and its adhesion strength was eval-

uated through a 180° lap shear test. To further validate adhesion performance, IDE/LiTFSI\_X/Y samples were tested with various substrates (Figure 4b; Figure S19, Supporting Information). The photograph on the right side of this figure shows the IDE/LiTFSI\_X/Y sample adhered to a glass substrate, successfully supporting a 2 kg weight. Figure 4c presents the adhesion strengths of IDE/LiTFSI\_X/Y samples on glass, PET, Cu, and Al substrates, among which the IDE/LiTFSI\_8/1 sample exhibited the highest adhesion strength of 320 kPa on glass. Adhesion strengths are presented as mean  $\pm$  S.E.M. ( $n = 3$ ). Statistical significance was assessed using the Kruskal-Wallis H-test. Exact  $p$ -values are provided in Table S6 (Supporting Information).

In Figure 4d, the peeling forces between IDE/LiTFSI\_X/Y samples and various substrates were measured using a 90° peeling test (Figure S20, Supporting Information). To limit crack tip deformation in IDE/LiTFSI\_X/Y samples, a rigid PET film with a thickness of 300  $\mu\text{m}$  was attached. Among the tested combinations, the IDE/LiTFSI\_8/1 sample displayed a peeling force per width ranging from 300–900  $\text{N m}^{-1}$  on glass, indicative of excellent adhesion performance. Peeling forces are presented as mean  $\pm$  S.E.M. ( $n = 3$ ). Statistical significance was assessed using the Kruskal-Wallis H-test. Exact  $p$ -values are provided in Table S7 (Supporting Information). Figure 4e illustrates the peeling process of the IDE/LiTFSI\_8/1 sample from the glass substrate. Figure 4f shows the adhesion mechanisms of IDE on various substrates through three types of interactions. In IDE, sulfonate groups form coordination bonds with metal atoms, and the imidazole groups engage in electrostatic interactions with glass, thereby causing ion-dipole interactions with PET. These interactions confirm the strong adhesion performance of the IDE with different substrates.

## 2.5. Resistive-Type Iontronic Sensors with IDE/LiTFSIs

Figure 5a shows a schematic of resistive-type iontronic sensors with IDE/LiTFSI\_X/Y for strain sensing. As shown in Figure 5b, the initial resistance value of the IDE/LiTFSI\_X/Y sensors exhibits a similar trend to the ionic conductivity behavior analyzed in Figure 2c. The initial resistances are presented as mean  $\pm$  S.E.M. ( $n = 3$ ). Statistical significance was assessed using the Kruskal-Wallis H-test. Exact  $p$ -values are provided in Table S8 (Supporting Information). An IDE/LiTFSI\_1/1 sensor exhibited the lowest resistance at 12  $\text{k}\Omega$  due to its excellent ionic conductivity. Figure S21 (Supporting Information) shows a schematic of the stability analysis of a resistive-type iontronic sensor by utilizing the weight-bearing properties of the IDE/LiTFSI\_X/Y sensor (IDE/LiTFSI\_X/Y size:  $2.0 \times 1.0 \times 0.1 \text{ cm}^3$ ). The IDE/LiTFSI\_X/Y sensor was covered with glass, and when a 5 kg weight was placed on top (Figure S21, Supporting Information), resistance did not change after 1 h (Figure 5c), indicating the stability of the resistive-type iontronic sensor.

The IDE/LiTFSI\_1/2 sensor, with the highest stretchability (100%), is suitable for resistive-type iontronic sensors, and its strain-sensing performance under deformation was investigated. When IDE/LiTFSI\_1/2 was stretched, its cross-sectional area decreased, resulting in a significant increase in resistance. The resistance changes ( $\Delta R/R_0$ ) of the resistive



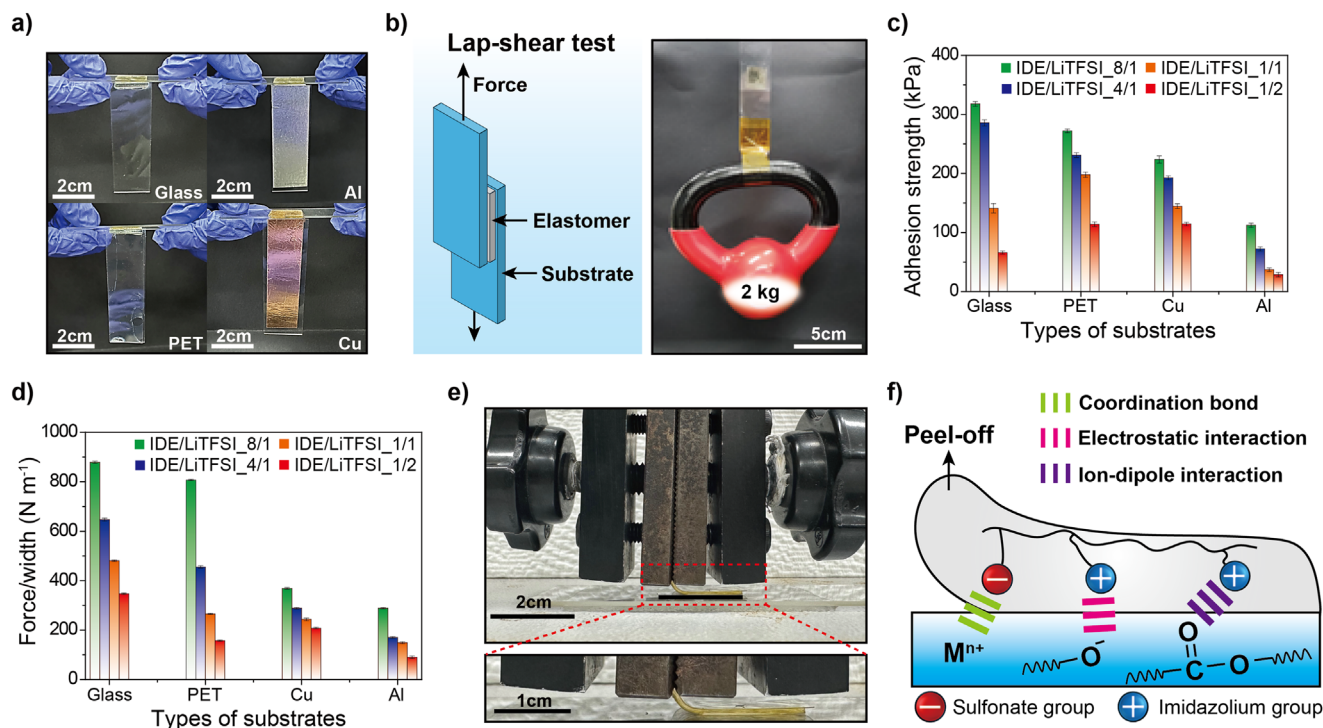


**Figure 4.** Adhesive property of IDE/LiTFSI\_X/Y. a) Strong adhesion photograph of glass, Al, PET, and Cu substrates with IDE/LiTFSI\_8/1. b) Schematic of the lap-shear test process and photographic demonstration of the high lap-shear strength to lift a weight of 2 kg (IDE/LiTFSI\_8/1). c) Maximum adhesion strength-displacement plot data obtained from the lap-shear tests of IDE/LiTFSI\_X/Y (IDE/LiTFSI\_X/Y size:  $2.0 \times 2.0 \times 0.1$  cm<sup>3</sup>) adhered to different substrates. Data are presented as mean  $\pm$  S.E.M. ( $n = 3$ ). Statistical significance was assessed using the Kruskal-Wallis H-test. Exact  $p$ -values are provided in Table S6 (Supporting Information). d) Force-displacement plot data obtained from the 90° peeling test of IDE/LiTFSI\_X/Y adhered to various substrates. Data are presented as mean  $\pm$  S.E.M. ( $n = 3$ ). Statistical significance was assessed using the Kruskal-Wallis H-test. Exact  $p$ -values are provided in Table S7 (Supporting Information). e) Photographs of the sample during the 90° peeling test. f) Schematic adhesion mechanism between IDE/LiTFSI\_X/Y and the substrates.

sensors were monitored within the strain range of 0%–100%. The gauge factor (GF), defined as the relative change in resistance with respect to the applied strain, can be used to evaluate sensor sensitivity. In Figure 5d, GF values of IDE/LiTFSI\_1/2 in the strain ranges of 0%–14%, 14%–56%, and 56%–100% were 2.17, 2.92, and 1.69, respectively, indicating high sensitivity of the strain sensors prepared from IDE/LiTFSI\_1/2. In cyclic stretch and release tests in the strain range of 20%–80% (Figure 5e), the IDE/LiTFSI\_1/2 sensor exhibited accurate and reversible resistance responsiveness. IDE/LiTFSI\_1/2 could detect stress across a wide range of strains and maintain resistance stability even after 400 cycles of stretching (Figure 5f). As a result, IDE/LiTFSI exhibited reversible and high resistance changes along with mechanical stability, demonstrating its suitability for stable iontronic applications under practical operating conditions.

## 2.6. Application of IDE/LiTFSI to ASSBs

The feasibility of IDE/LiTFSI\_1/1 as a solid electrolyte was evaluated using a Li||Li-symmetric cell at a current density of  $1.0 \text{ mA cm}^{-2}$  and a capacity of  $1.0 \text{ mAh cm}^{-2}$  (Figure 6a). Under these operating conditions, IDE/LiTFSI\_1/1 exhibited a stable and reliable Li plating/stripping cycling behavior owing to its im-

proved Li<sup>+</sup> conduction and superior mechanical strength. To provide additional evidence, we examined the structural changes of the Li metal anode before and after a repeated Li plating/stripping test (100 h). The IDE/LiTFSI\_1/1 electrolyte resulted in a nodular, dense, and uniform surface morphology on the Li metal anode (Figure S22, Supporting Information), suggesting that IDE/LiTFSI\_1/1 facilitated homogeneous Li<sup>+</sup> flux toward the anode while mitigating interfacial side reactions.<sup>[66,67]</sup> Furthermore, as shown in Figure 4, the strong interfacial adhesion properties of IDE/LiTFSI\_1/1 are expected to suppress dendritic Li growth by ensuring intimate and stable contact with the Li metal anode. The stable cyclability of the IDE/LiTFSI\_1/1-based cell was confirmed using EIS analysis (Figure 6b). A slight increase in cell resistance was observed during the cycling test, with the SEI resistance ( $R_{\text{SEI}}$ ) increasing from 62.24 to 80.23  $\Omega$  (after 100 h), and the charge transfer resistance ( $R_{\text{CT}}$ ) increasing from 14.2 to 16.3  $\Omega$  (after 100 h) (Table S9, Supporting Information). The ASSB with the IDE/LiTFSI\_1/1 exhibited a decent discharge rate capability at various current densities ranging from 0.2 to 2.0 C (Figure S23, Supporting Information). These results demonstrate the potential of IDE/LiTFSI\_1/1 as a promising polymer electrolyte for Li-metal anodes.

To explore the practical applicability of IDE/LiTFSI\_1/1, a full-cell pouch-type all-solid-state battery (ASSB) was fabricated in which IDE/LiTFSI\_1/1 functioned as both an ion-conducting



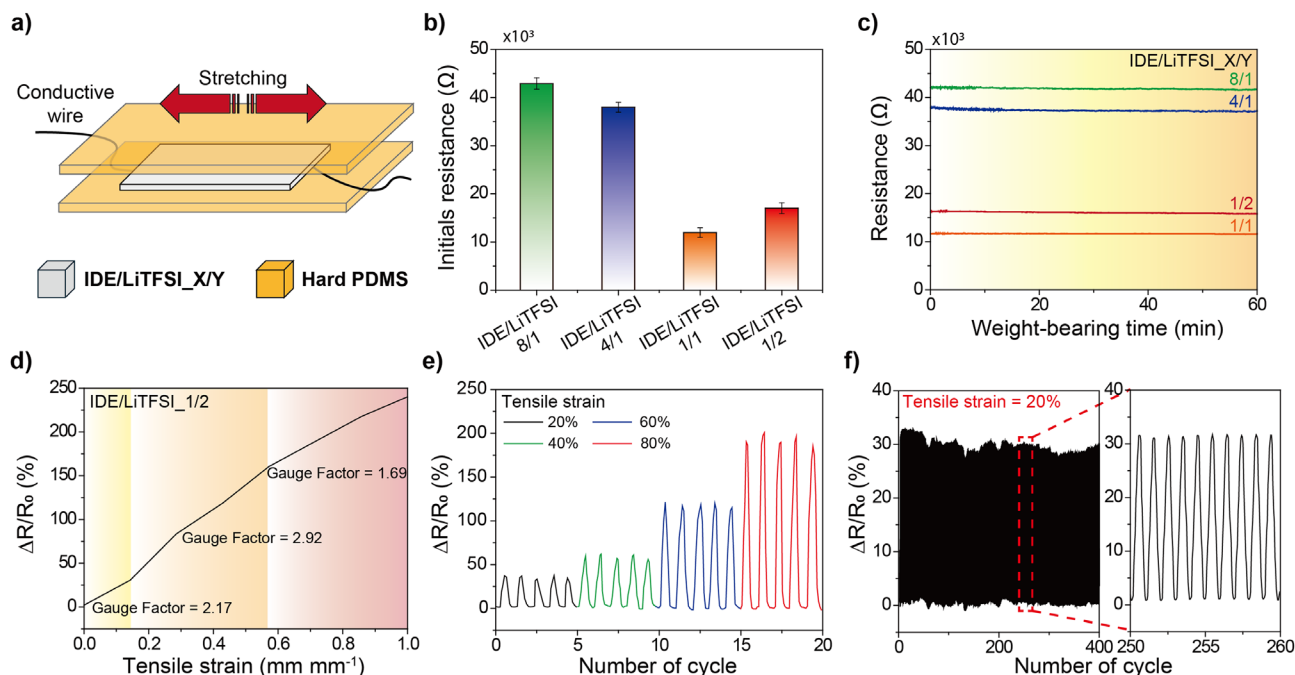


**Figure 5.** Resistive-type iontronic sensor for strain sensing properties of the IDE/LiTFSI sensor. a) Schematic of the resistive-type iontronic sensor for strain sensing. b) Electrical initial resistance plotting of IDE/LiTFSI\_X/Y. Data are presented as mean  $\pm$  S.E.M. ( $n = 3$ ). Statistical significance was assessed using the Kruskal-Wallis H-test. Exact p-values are provided in Table S8 (Supporting Information). c) The IDE/LiTFSI\_X/Y samples show stable resistance behavior for 1 h under a 5 kg load. d) GF at various tensile strains, reflecting the sensitivity of the sensor to external forces. e) Resistance change responses of a resistive-type iontronic sensor based on IDE/LiTFSI\_1/2 during continuous tensile deformation. f) Stable cyclic resistance changes of a resistive-type iontronic sensor based on IDE/LiTFSI\_1/2 under loading–unloading cycles at 20% deformation over 400 cycles.

separator membrane and a solid catholyte. The full cell consisted of an IDE/LiTFSI-embedded NCM811 cathode (areal capacity of  $4.0 \text{ mAh cm}^{-2}$ , comparable to commercial Li-ion battery cathodes<sup>[68]</sup>) || Li-metal anode (areal capacity of  $4.0 \text{ mAh cm}^{-2}$ , negative (N)/positive (P) capacity ratio = 1.0). The cell with the IDE/LiTFSI\_1/1 exhibited good rate capability across discharge current densities ranging from  $0.2 (= 0.8 \text{ mA cm}^{-2})$  to  $2.0 \text{ C}$  (Figure S23, Supporting Information). Under practical operating conditions ( $25^\circ\text{C}$ ,  $0.2 \text{ MPa}$ ), the cell exhibited stable cycling performance, retaining 88.1% of its initial capacity after 100 cycles at a high current density of  $1.0 \text{ C}$  (corresponding to  $4.0 \text{ mA cm}^{-2}$ ), (Figure 6c). Moreover, at an elevated temperature of  $60^\circ\text{C}$ , the cell maintained a capacity retention of 91.0% after 100 cycles (Figure S24, Supporting Information), indicating the excellent thermal and electrochemical stability of the IDE/LiTFSI\_1/1 electrolyte.

A key limitation of ASSBs that use inorganic solid electrolytes is their inherent mechanical stiffness,<sup>[69,70]</sup> which limits their practical application in flexible energy storage systems. In contrast, the use of IDE/LiTFSI\_1/1, a highly deformable polymer electrolyte, enabled physical flexibility in ASSBs (Figure S25, Supporting Information), which is due to the monolithic integration of cell components through in situ polymerization. To quantitatively investigate the mechanical flexibility of the ASSB, a pouch-type cell (dimensions:  $2.0 \times 2.0 \text{ cm}^2$ , capacity:  $4.0 \text{ mAh cm}^{-2}$ ) was fabricated and subjected to repeated bending cycles. The cell maintained stable charge/discharge profiles and cycling performance under practical operating conditions even after 100 bending cycles (bending radius: 5 mm, deformation

rate:  $30 \text{ mm min}^{-1}$ ) (Figure 6d). Additionally, the ASSB successfully powered an LED lamp after multiple bending cycles, further demonstrating its mechanical resilience (inset of Figure 6d).

Although inorganic solid electrolytes have been extensively studied for use in ASSBs, recent reports have raised concerns about the safety of ASSBs incorporating these electrolytes.<sup>[71,72]</sup> To assess the flame-retardant performance of IDE/LiTFSI\_1/1 as an alternative solid electrolyte, a cone calorimeter test was conducted (Figure S26, Supporting Information). The IDE/LiTFSI\_1/1 exhibited a low peak heat release rate (PHRR) of  $54.3 \text{ kW m}^{-2}$  and a total heat release (THR) of  $2.63 \text{ MJ m}^{-2}$ , indicating its inherently reduced flammability compared to conventional polymer-based electrolytes.<sup>[73,74]</sup> Also, to evaluate the safety performance of an ASSB containing IDE/LiTFSI\_1/1, a safety test was performed by horizontally cutting the cell in half. Remarkably, the ASSB continued to power the LED lamp without explosion or structural disintegration (inset of Figure 6e). Moreover, the cut cell maintained its functionality even when exposed to an open flame (Figure 6e), demonstrating the thermal stability and nonflammability of the IDE/LiTFSI\_1/1. These results highlight the potential of IDE/LiTFSI\_1/1 as a viable alternative to conventional inorganic solid electrolytes.

### 3. Conclusion

In summary, we demonstrated a novel IDE system that effectively integrates high ionic conductivity with superior mechanical robustness, thereby addressing critical challenges in the

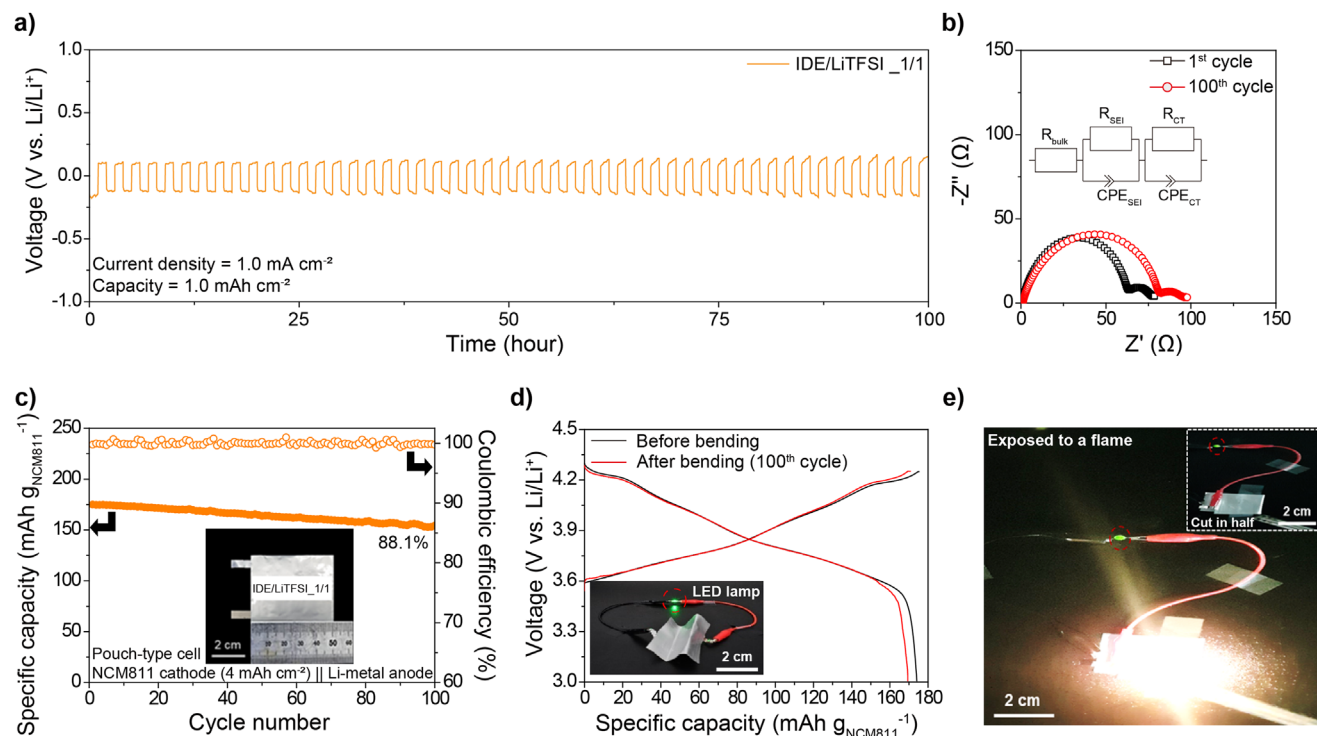


**Figure 6.** Energy storage application of the IDE/LiTFSI<sub>1/1</sub> to ASSBs composed of Li-metal anodes. a) Voltage profiles of the Li||Li symmetric cells with IDE/LiTFSI<sub>1/1</sub> at a current density of 1.0 mA cm<sup>-2</sup> and a capacity of 1.0 mAh cm<sup>-2</sup>. b) EIS spectra of Li||Li symmetric cells with the IDE/LiTFSI<sub>1/1</sub> after 1 and 100 cycles. c) Cycling performance of the pouch-type cell (length × width = 2 × 2 cm<sup>2</sup>) at a charge/discharge current density of 1.0 C (=4 mA cm<sup>-2</sup>)/1.0 C and a voltage range of 3.0–4.3 V at 25 °C. d) Charge/discharge voltage profiles (expressed as real capacities) of the ASSB with IDE/LiTFSI<sub>1/1</sub> before and after bending (bending radius = 5 mm and deformation rate = 30 mm min<sup>-1</sup>). The inset shows that the multiple-folded ASSB powered an LED lamp. e) Safety tests of the ASSB with IDE/LiTFSI<sub>1/1</sub>. It stably powered the LED lamp even after being vertically cut in half (inset) and exposed to flame.

advancement of ionic materials. A novel high-purity ID with ≈99% strong ionic bonding in the monomer state was synthesized based on the strong ionic bonds between imidazolium-based cationic monomers and sulfonate-based anionic monomers. ID was polymerized with a cross-linking moiety to form a network, resulting in a new mechanically robust and ionically conductive polymer (IDE), through the introduction of the LiTFSI salt. The resulting IDE/LiTFSI<sub>1/1</sub> exhibited good electrochemical properties, achieving a high ionic conductivity of 0.82 mS cm<sup>-1</sup> and a  $t_{\text{Li}^+}$  of 0.79, surpassing the performance of previously reported ionic elastomers. The intrinsic ionic bonding network within IDE/LiTFSI<sub>1/1</sub> contributes to its exceptional mechanical properties, with tensile strengths of 27.4 MPa and a Young's modulus of 211 MPa. In addition to its mechanical and electrochemical performance, IDE/LiTFSI demonstrated excellent adhesion to various substrates and functioned effectively as a strain sensor, exhibiting a GF of 2.92 and maintaining stable resistance over ≈400 cycles of repeated deformation. These characteristics highlight their potential for iontronic applications and energy storage technologies. Additionally, the pouch-type full cell with IDE/LiTFSI exhibited stable cyclability under constrained cell conditions. Overall, IDE/LiTFSI represents a versatile material platform with broad applicability in next-generation flexible iontronics and energy storage systems, providing a promising avenue for the development of high-performance ionic materials.

## 4. Experimental Section

**Materials:** 1-Butylimidazole (98%, Sigma-Aldrich), 2-bromoethyl acrylate (94%, Alfa), acetonitrile (≥99.5%, Sigma-Aldrich), dichloromethane (DCM, ≥99.8%, Sigma-Aldrich), deionized H<sub>2</sub>O (Sigma-Aldrich), 3-sulfopropyl acrylate potassium salt (K[SPA], Sigma-Aldrich), and bis(trifluoro methane)sulfonimide lithium salt (LiTFSI, ≥99.95%, Sigma-Aldrich). LiNi<sub>0.8</sub>Co<sub>0.1</sub>Mn<sub>0.1</sub>O<sub>2</sub> (NCM811, LG energy solution), N-methyl-2-pyrrolidone (NMP, Sigma-Aldrich), and Li-metal foil (Honjo Metal Co., Ltd., thickness 20 μm).

**Synthesis of IDs:** Under N<sub>2</sub> atmosphere, 5.0 g of 2-bromoethyl acrylate and 3.64 g of 1-butylimidazole were mixed in 30 mL of fresh acetonitrile and stirred overnight at 65 °C. After the reaction, the acetonitrile was removed using a rotary evaporator. 1-[2-acryloyloxyethyl]-3-butyl imidazolium bromide ([AEBI]Br) was extracted using deionized water, followed by washing with dichloromethane at least five times. After washing, deionized water was removed via a vacuum oven at 70 °C. Then, 2.351 g of [AEBI]Br was dissolved in 30 g of acetonitrile, and 2.46 g of K[SPA], with the same molar amount as [AEBI]Br, and stirred overnight at 65 °C. After the reaction, the precipitate of 1.23 g of the KBr precipitate was removed using filter paper, and the resulting transparent solution was concentrated using a rotary evaporator to remove acetonitrile. The [AEBI][SPA] dimer produced by the reaction weighed 3.46 g, resulting in a yield of 98.38%. The [AEBI][SPA] dimer was sealed and stored in a glove box.

**Preparation of IDEs:** [AEBI][SPA] dimer (0.2 g), PEGDA (molecular weight: 700 g mol<sup>-1</sup>, 2 wt.%), and HOMPP (photo initiator, 2 wt.%) were dissolved in ethanol or DMF (0.1 g). The [AEBI][SPA] dimer solution was poured into a poly(dimethyl siloxane) (PDMS) mold and polymerized for 120 s using UV radiation to proceed with gelation. The polymerized [AEBI][SPA] dimer was dried in a vacuum oven at 65 °C for more than 24 h to remove the solvent.

**Thermal and Mechanical Characterization:** The mechanical properties of the IDE and IDE/LiTFSI samples were tested using a tensile machine (Mechmesine, 50 N load cell) at room temperature (25 °C). The dog bone-shaped samples were subjected to monotonic tensile testing at a tensile rate of 60 mm min<sup>-1</sup>. Young's modulus was defined as the initial slope of the tensile stress-strain curve. The IDE/LiTFSI\_1/1 sample was notched and obtained by cutting a 4 mm long linear notch from the edge to the center using a sharp blade. The corresponding fracture energy ( $\Gamma$ ) value was obtained by multiplying the integrated area of the stress-strain curve of the unnotched sample, from the initial loading position to the critical strain of crack propagation ( $\epsilon_c$ ) of the notched sample, by the initial distance between the clamps. In this equation,  $A$  represents the fracture surface area, and  $F$  denotes the applied stress. The calculation formula is defined as follows:  $\Gamma = A^{-1} \times \int_0^{\epsilon_c} F d\epsilon$ . The rheological properties of the IDE/LiTFSI samples were measured with an MCR 702e (Anton Paar) instrument (1% strain) using a plate geometry with a diameter of 4 mm and a sample thickness greater than 1 mm. The thermal properties of the IDE and IDE/LiTFSI samples were characterized by DSC (Discovery DSC 250 Auto, TA instruments), with a heating and cooling rate of 10 °C min<sup>-1</sup>. The residual solvent measurement of the IDE and IDE/LiTFSI samples was characterized by TGA (SDT 500, TA instruments) with a heating range of 30–400 °C. GPC tests were conducted using a Tosoh (EcoSEC HLC-8420 GPC) system. 0.1 M NaNO<sub>3</sub> was used as the mobile phase at a flow rate of 1 mL min<sup>-1</sup>.

**Structural and Physicochemical Characterization:** <sup>1</sup>H NMR and <sup>13</sup>C NMR (Bruker, Avance III HD 300) spectra of the IDs and IDEs were recorded on Bruker instruments operating at 300 and 125 MHz, respectively. D<sub>2</sub>O was used as the NMR solvent depending on the solubility of the IDs and IDEs. <sup>1</sup>H and <sup>13</sup>Li NMR (Bruker BioSpin, Avance III HD500) spectra were used to verify the diffusion coefficient using Diffusion-Ordered Spectroscopy (DOSY). These measurements were conducted at the Chronic and Metabolic Diseases Research Center, Sookmyung Women's University. UV-vis spectra were obtained using a Cary 5000 UV-vis spectrometer. ATR-FTIR spectroscopy was performed using a Vertex 70 spectrometer (Bruker). The surface morphology and height deviation of the non-pressed electrodes were characterized by laser scanning confocal microscopy (FV1000, Carl Zeiss), in which the height deviation was the difference between the observed height of the electrolyte and its average height. Powder XRD patterns were collected using a Rigaku MiniFlex600 diffractometer with Cu K $\alpha$  radiation ( $\lambda = 1.5406$  Å). For the XRD analysis, XRD cells containing the samples were mounted on an XRD diffractometer and measured at 40 kV and 15 mA. The surface and cross-sectional morphologies of the electrodes were investigated using field-emission scanning electron microscopy (FE-SEM; S-4800, Hitachi).

**Electrochemical Characterization:** The  $\xi$  is typically determined by comparing ionic conductivity from EIS with molar conductivity from PFG-NMR. EIS is a rapid experimental method for determining the ionic conductivity of a system by measuring the impedance across a given cell. Unlike the conductivity calculated using the Nernst-Einstein equation, only “free ions” contributing to the ionic conductivity of the system can be measured using this method. Therefore, one can estimate the  $\xi$  by taking the ratio of the molar conductivity from EIS measurements to the molar conductivity from PFG-NMR and the Nernst-Einstein equation:

$$\xi = \frac{\lambda_{\text{EIS}}}{C_{\text{IL}} \Lambda_{\text{NE}}} \quad (1)$$

where  $\lambda_{\text{EIS}}$  is the ionic conductivity in EIS, and  $C_{\text{IL}}$  is the molar concentration of ID per unit volume. The Nernst-Einstein equation (Equation 2)

relates the self-diffusion coefficients ( $D$ ) of the [AEBI]<sup>+</sup> ( $D_+$ ) and [SPA]<sup>-</sup> ( $D_-$ ) to the molar conductivity ( $\Lambda_{\text{NE}}$ ):

$$\Lambda_{\text{NE}} = \frac{N_A e^2}{k_B T} (z_+^2 D_+ + z_-^2 D_-) \quad (2)$$

where  $N_A$  is Avogadro's number,  $e$  is the charge of an electron,  $k_B$  is the Boltzmann constant,  $T$  is the absolute temperature, and  $z_+$  and  $z_-$  are the [AEBI]<sup>+</sup> and [SPA]<sup>-</sup> charges, respectively. The self-diffusion coefficients  $D_+$  and  $D_-$  are determined using PFG-NMR, which detects atomic nuclei (e.g., <sup>13</sup>Li and <sup>1</sup>H) without distinguishing ion pairing or aggregation. Thus,  $D_+$  and  $D_-$  determined by NMR, represent the average self-diffusion of all ions in a given system. The  $D$  of the [AEBI]<sup>+</sup> and the [SPA]<sup>-</sup> measured by PFG-NMR were  $8.881 \times 10^{-12}$  and  $5.772 \times 10^{-12}$  m<sup>2</sup> s<sup>-1</sup>, respectively. As a result, the  $\Lambda_{\text{NE}}$  calculated using Equation 2 is  $6.39 \times 10^{34}$  e<sup>2</sup> s kg<sup>-1</sup> mol<sup>-1</sup>. Additionally, the  $\Lambda_{\text{EIS}}$  and  $C_{\text{IL}}$  of ID measured by EIS are 0.0549 mS cm<sup>-1</sup> and  $0.95 \times 10^{-3}$  mol cm<sup>-3</sup>, respectively. The ionic conductivities of the electrodes were estimated by EIS analysis in the frequency range of 10<sup>-2</sup> to 10<sup>6</sup> Hz and an applied amplitude of 10 mV using a potentiostat (VSP Classic, Bio-Logic). Impedance was measured from 25 to 80 °C. Ionic conductivity was determined using the following equation:

$$\sigma = \frac{L}{RA} \quad (3)$$

where  $L$  is the pellet thickness,  $R$  is the resistance, and  $A$  is the area of contact with the electrode. The activation energy ( $E_a$ ) of ionic conduction was determined from the slope of the Arrhenius plot. Electrochemical stability windows of the electrolytes were evaluated by linear sweep voltammetry (LSV) analysis at a scan rate of 0.1 mV s<sup>-1</sup>, in which a carbon electrode was used as the working electrode. The  $t_{\text{Li}^+}$  was evaluated using a potentiostatic polarization method. DC polarization through a Li<sup>+</sup> non-blocking symmetric cell and its sequential EIS before and after polarization were analyzed to determine  $t_{\text{Li}^+}$ .

$$t_{\text{Li}^+} = \frac{I_s (\Delta V - I_0 R_0)}{I_0 (\Delta V - I_s R_s)} \quad (4)$$

where  $V$  is the applied potential,  $I_0$  and  $R_0$  are the initial current and resistance, respectively, and  $I_s$  and  $R_s$  are the steady-state current and resistance, respectively, after polarization. The EIS fitting method for an electrochemical system was conducted on an equivalent electrical circuit consisting of common passive components (such as resistances and capacitances) and other more complicated (referred to as distributed) elements connected using potentiostat software (VSP Classic, Bio-Logic) to simulate the impedance data on a model circuit. The Li-metal anode cycle test was conducted using Li||Li symmetric cells at a current density of 1.0 mA cm<sup>-2</sup> and an areal capacity of 1.0 mAh cm<sup>-2</sup> at 25 °C. The charge/discharge performance of the cells was investigated using a cycle tester (PNE Solution).

**Fabrication of Resistive-Type Iontronic Sensors:** Hard PDMS was mixed with a PDMS base/PDMS curing agent = 10/1 (w/w). The mixed hard PDMS solution was degassed in a vacuum oven to remove internal bubbles and cured overnight at 65 °C (thickness = 1 mm). The IDE/LiTFSI was transferred onto hard PDMS, and Cu tape was attached to both ends of the IDE/LiTFSI. The contact area between the Cu tape and the IDE/LiTFSI was  $0.2 \times 1.0$  cm<sup>2</sup>. The IDE/LiTFSI with the Cu tape was then encapsulated with the remaining hard PDMS, and the top and bottom hard PDMS layers were strongly bonded using an O<sub>2</sub> plasma system.

**Fabrication of the Electrodes and ASSB Full Cells:** Cathode slurries were prepared with a composition of NCM811/carbon black/polyvinylidene fluoride (PVDF) = 96/2/2 (w/w/w). PVDF was used as the sole binder for the cathode after dissolution in NMP for 12 h. The concentration of the binder solution was standardized to 10 wt.%. The cast cathode slurry was vacuum-dried at 120 °C for 12 h, followed by calendaring at 60 °C. The cathodes were fabricated by casting a slurry onto an Al current collector. Thereafter, the cast cathode slurry was vacuum-dried at 80 °C for 12 h, followed by calendaring at 120 °C. The areal mass loading of active materials



in the casted cathode was  $21.0 \text{ mg cm}^{-2}$ . A thin Li metal foil was used as the anode in the full cell. The pouch-type cell (composed of NCM811 cathode ( $4.0 \text{ mAh cm}^{-2}$ ))||Li-metal anode, N/P ratio = 1.0) was fabricated using an Al pouch film as a packaging substance in a dry room with a dew point of  $-60^\circ\text{C}$ . The electrochemical performance of the pouch-type cell was evaluated at  $25^\circ\text{C}$  under a fixed pressure set as 200 kPa.

**Statistical Analysis:** All quantitative measurements, including mechanical properties (tensile strength, stretchability, Young's modulus, and toughness), absolute diffusion constant, initial resistance, lap-shear test, and  $90^\circ$  peeling test, were conducted using four different IDE/LiTFSI compositions (8/1, 4/1, 1/1, and 1/2), with three independent replicates per composition group ( $n = 3$  for each IDE/LiTFSI ratio). Data are presented as mean  $\pm$  standard error of the mean (S.E.M.). Due to the small sample size and the potential for non-normal data distributions, statistical significance was evaluated using the non-parametric Kruskal-Wallis H-test. A  $p$ -value less than 0.05 was considered statistically significant. All statistical analyses were performed using Microsoft Excel 365. Exact  $p$ -values and test statistics are provided in the Supporting Information. The Kruskal-Wallis H test was used to assess statistically significant differences among the IDE/LiTFSI samples with varying  $\text{Li}^+$  salt ratios (8/1, 4/1, 1/1, and 1/2). The test statistics were calculated as

$$H = \frac{12}{N(N+1)} \sum_{i=1}^k \frac{R_i^2}{n_i} - 3(N+1) \quad (5)$$

where  $k$  is the number of groups,  $n_i$  is the number of samples in group  $i$ ,  $R_i$  is the sum of ranks for group  $i$ , and  $N$  is the total number of observations. A  $p$ -value  $< 0.05$  was considered statistically significant. Statistical calculations were performed using OriginPro 2023 (OriginLab Corporation) and verified by manual ranking where needed.

## Supporting Information

Supporting Information is available from the Wiley Online Library or from the author.

## Acknowledgements

T.K. and K.-S.O. contributed equally to this study. This study was supported by a grant from the National Research Foundation of Korea (NRF) funded by the Korean government (MEST) (RS-2023-00208577), by the Nano & Material Technology Development Program through the National Research Foundation of Korea (NRF) funded by the Ministry of Science and ICT (RS-2024-00451891 and RS-2024-00416938), by the Basic Science Research Program (RS-2024-00344021) through a National Research Foundation of Korea (NRF) grant from the Korean Government (MSIT).

## Conflict of Interest

The authors declare no conflict of interest.

## Data Availability Statement

The data that support the findings of this study are available from the corresponding author upon reasonable request.

## Keywords

all-solid-state batteries, ionic conductivity, ionic dimer elastomer, mechanical strength, resistive-type iontronic sensor

Received: May 7, 2025  
Revised: July 2, 2025  
Published online:

- [1] M. W. M. Tan, H. Wang, D. Gao, P. Huang, P. S. Lee, *Chem. Soc. Rev.* **2024**, 53, 3485.
- [2] J. Li, J. Cao, B. Lu, G. Gu, *Nat. Rev. Mater.* **2023**, 8, 604.
- [3] Z. Lei, W. Zhu, X. Zhang, X. Wang, P. Wu, *Adv. Funct. Mater.* **2021**, 31, 2008020.
- [4] H. Qiao, S. Sun, P. Wu, *Adv. Mater.* **2023**, 35, 2300593.
- [5] H. Ye, B. Wu, S. Sun, P. Wu, *Nat. Commun.* **2024**, 15, 885.
- [6] Y. Luo, J. Li, Q. Ding, H. Wang, C. Liu, J. Wu, *Nano-Micro Lett.* **2023**, 15, 136.
- [7] Z. Li, J. Lu, T. Ji, Y. Xue, L. Zhao, K. Zhao, B. Jia, B. Wang, J. Wang, S. Zhang, Z. Jiang, *Adv. Mater.* **2024**, 36, 2306350.
- [8] S. X. Drakopoulos, J. Wu, S. M. Maguire, S. Srinivasan, K. Randazzo, E. C. Davidson, R. D. Priestley, *Progress Polymer Sci.* **2024**, 156, 101870.
- [9] C. Li, K. Zhang, X. Cheng, J. Li, Y. Jiang, P. Li, B. Wang, H. Peng, *Progress Polymer Sci.* **2023**, 143, 101714.
- [10] C. Lu, H. Jiang, X. Cheng, J. He, Y. Long, Y. Chang, X. Gong, K. Zhang, J. Li, Z. Zhu, J. Wu, J. Wang, Y. Zheng, X. Shi, L. Ye, M. Liao, X. Sun, B. Wang, P. Chen, Y. Wang, H. Peng, *Nature* **2024**, 629, 86.
- [11] X. Lu, Y. Wang, X. Xu, B. Yan, T. Wu, L. Lu, *Adv. Energy Mater.* **2023**, 13, 2301746.
- [12] A. M. M. Hasan, S. Bose, R. Roy, J. D. Marquez, C. Sharma, J. C. Nino, K. O. Kirlikovali, O. K. Farha, A. M. Evans, *Adv. Mater.* **2024**, 36, 2405924.
- [13] U. H. Choi, P. L. Handayani, Y. H. Song, T. Kim, A. Han, R. H. Colby, *Macromolecules* **2023**, 56, 3393.
- [14] H. Wang, B. Liu, D. Chen, Z. Wang, H. Wang, S. Bao, P. Zhang, J. Yang, W. Liu, *Mater. Horiz.* **2024**, 11, 2628.
- [15] H. Zhang, N. He, B. Wang, B. Ding, B. Jiang, D. Tang, L. Li, *Adv. Mater.* **2023**, 35, 230098.
- [16] J. Jing, B. Yao, W. Sun, J. Chen, J. Xu, J. Fu, *Angew. Chem., Int. Ed.* **2024**, 136, 202410693.
- [17] R. Nasser, N. Bouzari, J. Huang, *Nat. Commun.* **2023**, 14, 6108.
- [18] C.-C. Yan, W. Li, Z. Liu, S. Zheng, Y. Hu, Y. Zhou, J. Guo, X. Ou, Q. Li, J. Yu, L. Li, M. Yang, Q. Liu, F. Yan, *Adv. Funct. Mater.* **2024**, 34, 2314408.
- [19] Z. Yu, Y. Zhao, K. Zhao, T. Zhou, C. Ye, *Chem. Eng. J.* **2024**, 499, 156113.
- [20] W. Zhan, J. Zhang, Q. Zhang, Z. Ye, B. Li, C. Zhang, Z. Yang, L. Xue, Z. Zhang, F. Ma, N. Peng, Y. Lyu, Y. Su, M. Liu, X. Zhang, *Mater. Horiz.* **2024**, 11, 4159.
- [21] J. Chen, Y. Gao, L. Shi, W. Yu, Z. Sun, Y. Zhou, S. Liu, H. Mao, D. Zhang, T. Lu, Q. Chen, D. Yu, S. Ding, *Nat. Commun.* **2022**, 13, 4868.
- [22] H. Xiang, X. Li, B. Wu, S. Sun, P. Wu, *Adv. Mater.* **2023**, 35, 2209581.
- [23] W. Zhu, B. Wu, Z. Lei, P. Wu, *Adv. Mater.* **2024**, 36, 2313127.
- [24] L. Yu, C. Huang, Y. Gong, S. Zheng, P. Zhou, X. Zhang, Z. Zou, X. Lyu, *Macromolecules* **2024**, 57, 2339.
- [25] Q. Li, W. Li, Z. Liu, S. Zheng, X. Wang, J. Xiong, F. Yan, *Adv. Mater.* **2024**, 36, 2311214.
- [26] L. Li, X. Wang, S. Gao, S. Zheng, X. Zou, J. Xiong, W. Li, F. Yan, *Adv. Mater.* **2024**, 36, 2308547.
- [27] B. Yiming, Y. Han, Z. Han, X. Zhang, Y. Li, W. Lian, M. Zhang, J. Yin, T. Sun, Z. Wu, T. Li, J. Fu, Z. Jia, S. Qu, *Adv. Mater.* **2021**, 33, 2006111.
- [28] Q. Cui, X. Huang, X. Dong, H. Zhao, X. Liu, X. Zhang, *Chem. Mater.* **2022**, 34, 10778.
- [29] L. Peng, L. Hou, P. Wu, *Adv. Mater.* **2023**, 35, 2211342.
- [30] L. D. Blackman, P. A. Gunatillake, P. Cass, K. E. S. Locock, *Chem. Soc. Rev.* **2019**, 48, 757.
- [31] T. L. Sun, T. Kurokawa, S. Kuroda, A. B. Ihsan, T. Akasaki, K. Sato, M. d. A. Haque, T. Nakajima, J. P. Gong, *Nat. Mater.* **2013**, 12, 932.
- [32] S. Mogurampelly, J. R. Keith, V. Ganesan, *J. Am. Chem. Soc.* **2017**, 139, 9511.
- [33] X. Ming, Y. Sheng, L. Yao, X. Li, Y. Huang, H. Zhu, Q. Zhang, S. Zhu, *Chem. Eng. J.* **2023**, 463, 142439.



- [34] Y. Huang, L. Xiao, J. Zhou, T. Liu, Y. Yan, S. Long, X. Li, *Adv. Funct. Mater.* **2021**, 31, 2103917.
- [35] Y. Zhang, Q. Hu, S. Yang, T. Wang, W. Sun, Z. Tong, *Macromolecules* **2021**, 54, 5218.
- [36] T. Long, Y. Li, X. Fang, J. Sun, *Adv. Funct. Mater.* **2018**, 28, 1804416.
- [37] H. Kim, S. M. Kong, J. A. Kim, G. Yoon, Y. H. Na, S. K. Kim, *Chem. Eng. J.* **2023**, 477, 147189.
- [38] H. Zhang, X. Jiang, S. Wu, X. Chu, T. Xiang, *ACS Appl. Energy Mater.* **2024**, 7, 499.
- [39] J. E. Potaufoux, R. Tavernier, J. Odent, J. M. Raquez, *Macromolecules* **2024**, 57, 7884.
- [40] Z. Chu, K. He, S. Huang, W. Zhang, X. Li, K. Cui, *Macromol. Rapid Commun.* **2024**, 45, 2400327.
- [41] X. Li, K. Cui, Y. Zheng, Y. N. Ye, C. Yu, W. Yang, T. Nakajima, J. P. Gong, *Sci. Adv.* **2023**, 9, 6856.
- [42] X. Li, F. Luo, T. L. Sun, K. Cui, R. Watanabe, T. Nakajima, J. P. Gong, *Macromolecules* **2023**, 56, 535.
- [43] J. Guo, S. Wu, Y. Wang, J. Huang, H. Xie, S. Zhou, *Mater. Horiz.* **2022**, 9, 3039.
- [44] X. Li, K. Cui, T. Kurokawa, Y. N. Ye, T. L. Sun, C. Yu, C. Creton, J. P. Gong, *Sci. Adv.* **2021**, 7, 8210.
- [45] Q. Hu, Y. Zhang, T. Wang, W. Sun, Z. Tong, *Macromol. Rapid Commun.* **2021**, 42, 2000747.
- [46] Y. Zhang, J. Liao, T. Wang, W. Sun, Z. Tong, *Adv. Funct. Mater.* **2018**, 28, 1707245.
- [47] A. B. Ihsan, T. L. Sun, T. Kurokawa, S. N. Karobi, T. Nakajima, T. Nonoyama, C. K. Roy, F. Luo, J. P. Gong, *Macromolecules* **2016**, 49, 4245.
- [48] K. Cui, T. L. Sun, T. Kurokawa, T. Nakajima, T. Nonoyama, L. Chen, J. P. Gong, *Soft Matter* **2016**, 12, 8833.
- [49] L. Wang, H. Wang, H. Yu, F. Luo, J. Li, H. Tan, *RSC Adv.* **2016**, 6, 114532.
- [50] F. Luo, T. L. Sun, T. Nakajima, D. R. King, T. Kurokawa, Y. Zhao, A. B. Ihsan, X. Li, H. Guo, J. P. Gong, *Macromolecules* **2016**, 49, 2750.
- [51] J. E. Park, H. S. Kang, M. Koo, C. Park, *Adv. Mater.* **2020**, 32, 2002178.
- [52] O. Nordness, J. F. Brennecke, *Chem. Rev.* **2020**, 120, 12873.
- [53] C. C. Huang, M. X. Du, B. Q. Zhang, C. Y. Liu, *Macromolecules* **2022**, 55, 3189.
- [54] N. L. Benbow, J. L. Webber, P. Pawlitzak, D. A. Sebben, T. T. M. Ho, J. Vongsivut, M. J. Tobin, M. Krasowska, D. A. Beattie, *Sci. Rep.* **2018**, 8, 17804.
- [55] T. Rajkumar, G. R. Rao, *Mater. Chem. Phys.* **2008**, 112, 853.
- [56] D. Zhang, Y. Liu, S. Yang, J. Zhu, H. Hong, S. Li, Q. Xiong, Z. Huang, S. Wang, J. Liu, C. Zhi, *Adv. Mater.* **2024**, 36, 2401549.
- [57] P. Shi, J. Ma, M. Liu, S. Guo, Y. Huang, S. Wang, L. Zhang, L. Chen, K. Yang, X. Liu, Y. Li, X. An, D. Zhang, X. Cheng, Q. Li, W. Lv, G. Zhong, Y.-B. He, F. Kang, *Nat. Nanotechnol.* **2023**, 18, 602.
- [58] Y. F. Huang, T. Gu, G. Rui, P. Shi, W. Fu, L. Chen, X. Liu, J. Zeng, B. Kang, Z. Yan, F. J. Stadler, L. Zhu, F. Kangac, Y.-B. He, *Energy Environ. Sci.* **2021**, 14.
- [59] V. Bocharova, A. P. Sokolov, *Macromolecules* **2022**, 55, 4141.
- [60] B. A. Paren, N. Nguyen, V. Ballance, D. T. Hallinan, J. G. Kennemur, K. I. Winey, *Macromolecules* **2022**, 55, 4692.
- [61] R.-Y. Wang, S. Jeong, H. Ham, J. Kim, H. Lee, C. Y. Son, M. J. Park, *Adv. Mater.* **2023**, 35, 2203413.
- [62] W. Li, S. Zheng, X. Zou, Y. Ren, Z. Liu, W. Peng, X. Wang, D. Liu, Z. Shen, Y. Hu, J. Guo, Z. Sun, F. Yan, *Adv. Funct. Mater.* **2022**, 32, 2207348.
- [63] W. Li, L. Li, S. Zheng, Z. Liu, X. Zou, Z. Sun, J. Guo, F. Yan, *Adv. Mater.* **2022**, 34, 2203049.
- [64] L. Bai, Y. Jin, X. Shang, H. Jin, W. Zeng, L. Shi, *Chem. Eng. J.* **2023**, 456, 141082.
- [65] X. He, Z. Zhu, G. Wen, S. Lv, S. Yang, T. Hu, Z. Cao, Y. Ji, X. Fu, W. Yang, Y. Wang, *Adv. Mater.* **2024**, 36, 2307599.
- [66] K.-S. Oh, J.-H. Kim, S.-H. Kim, D. Oh, S.-P. Han, K. Jung, Z. Wang, L. Shi, Y. Su, T. Yim, S. Yuan, S.-Y. Lee, *Adv. Energy Mater.* **2021**, 11, 2101813.
- [67] K.-S. Oh, S. Park, J.-S. Kim, Y. Yao, J.-H. Kim, J. Guo, D.-H. Seo, S.-Y. Lee, *ACS Energy Lett.* **2023**, 8, 2463.
- [68] J. H. Kim, J. M. Kim, S. K. Cho, N. Y. Kim, S. Y. Lee, *Nat. Commun.* **2022**, 13, 2541.
- [69] A. Banerjee, X. Wang, C. Fang, E. A. Wu, Y. S. Meng, *Chem. Rev.* **2020**, 120, 6878.
- [70] Y.-G. Lee, S. Fujiki, C. Jung, N. Suzuki, N. Yashiro, R. Omoda, D.-S. Ko, T. Shiratsuchi, T. Sugimoto, S. Ryu, J. H. Ku, T. Watanabe, Y. Park, Y. Aihara, D. Im, I. T. Han, *Nat. Energy* **2020**, 5, 299.
- [71] S. Lee, Y. Kim, C. Park, J. Kim, J.-S. Kim, H. Jo, C. J. Lee, S. Choi, D.-H. Seo, S.-K. Jung, *ACS Energy Lett.* **2024**, 9, 1369.
- [72] T. Kim, K. Kim, S. Lee, G. Song, M. S. Jung, K. T. Lee, *Chem. Mater.* **2022**, 34, 9159.
- [73] M. Zhang, M. B. Gomes, A. Yusuf, G.-Z. Yin, C.-C. Sun, D.-Y. Wang, *Eur. Polym. J.* **2024**, 215, 113246.
- [74] B. Chen, H. Huang, Y. Wang, Z. Shen, L. Li, Y. Wang, X. Wang, X. Li, Y. Wang, *ChemElectroChem* **2022**, 9, 202101277.